Texture Analysis of Aggressive and Nonaggressive Lung Tumor CE CT Images

Omar S. Al-Kadi*, *Member, IEEE*, and D. Watson

***Abstract*—This paper presents the potential for fractal analysis of time sequence contrast-enhanced (CE) computed tomography (CT) images to differentiate between aggressive and nonaggressive malignant lung tumors (i.e., high and low metabolic tumors). The aim is to enhance CT tumor staging prediction accuracy through identifying malignant aggressiveness of lung tumors. As branching of blood vessels can be considered a fractal process, the research examines vascularized tumor regions that exhibit strong fractal characteristics. The analysis is performed after injecting 15 patients with a contrast agent and transforming at least 11 time sequence CE CT images from each patient to the fractal dimension and determining corresponding lacunarity. The fractal texture features were averaged over the tumor region and quantitative classification showed up to 83.3% accuracy in distinction between advanced (aggressive) and early-stage (nonaggressive) malignant tumors. Also, it showed strong correlation with corresponding lung tumor stage and standardized tumor uptake value of fluorodeoxyglucose as determined by positron emission tomography. These results indicate that fractal analysis of time sequence CE CT images of malignant lung tumors could provide additional information about likely tumor aggression that could potentially impact on clinical management decisions in choosing the appropriate treatment procedure.**

***Index Terms*—Fractal dimension (FD), lacunarity, texture analysis, tumor aggression.**

I. Introduction

COMPUTED TOMOGRAPHY (CT) is one of the best imaging techniques for soft tissue imaging behind bone structures [1]. A modern multislice CT machine enables the rapid acquisition of precise sets of successive images with very high resolution supporting a more confident diagnosis. Multislice CT images having millimeter slice thickness and high spatial resolution, with fast acquisition times, minimizes artifacts due to abdominal movement and enables the clear visualization of anatomical features and structures for the purpose of anatomical texture analysis. Yet, conventional anatomical imaging of lung cancers gives little indication as to tumor aggression apart from size (i.e., big is bad) and ground glass (i.e., favorable) opacification, while the status of the tumor vasculature is related to tumor aggression and survival [2]. Assessment of lesion heterogeneity and/or surface irregularity on CT and chest radiographs, including fractal analysis, can distinguish between normal tissue and tumors [3]–[10]. Nevertheless, commercial systems for computer-assisted diagnosis of lung nodules are available for lesion detection and not for characterization and identification of aggressiveness through examining image texture.

Texture analysis is concerned with the study of the variation in intensity of image elements (pixel) values acquired under certain conditions. From a medical imaging perspective, physical quantities at scales smaller than the scales of interest can be analyzed for proper classification [11]. In this research, the image intensities are transformed to the fractal dimension (FD) domain for the purpose of texture analysis of the fractal features (i.e., fractal analysis). The process of fractal analysis has many applications including image compression and segmentation as well as in image processing. Being able to extract useful otherwise hidden information through digitally processing medical images is an important tool for physicians to support the accurate diagnosis without the need for biopsies—a process that can be unpleasant for patients and requires time, effort, and incurs additional costs. The ability to predict the type of tumor with good accuracy from the image could be very advantageous.

Many studies have applied fractal analysis for different imaging modalities using different approaches for the calculation of FD in cases where expert radiologists may have difficulty in identifying features. A number of studies reported successful results making use of fractals in texture analysis that are summarized in Table I.

Most studies were primarily concerned with distinguishing between normal and abnormal cases. This research is more concerned with lung tumor classification by determining FD feature vectors for regions of interest (ROIs), and using these vectors as predictors for tumor aggression. So far, investigation of abnormal cases only (i.e., aggressiveness of malignancies) and classifying them according to their aggressiveness and determining how FD relates to real medical key indicators was not investigated before.The aim is to improve tumor stage prediction accuracy and not simply differentiating between normal and abnormal tissue. Amongst malignant lesions, the propensity for spread of tumor to other organs is variable. More aggressive lesions are associated with earlier and more extensive tumor spread. The extent of spread is described by the tumor stage, with higher stages reflecting more extensive disease. The ability of conventional CT to accurately determine the stage of lung cancer is limited in comparison to functional imaging techniques such as fluorodeoxyglucose positron emission tomography (FDG-PET) [12]. Furthermore, FDG-PET can assess tumor metabolic activity that also tends to be greater in aggressive

Manuscript received August 9, 2007; revised January 10, 2008. This work was supported by the University of Jordan, Amman, Jordan, under Scholarship 8/2214/145. *Asterisk indicates corresponding author.*

*O. S. Al-Kadi is with the Department of Informatics, University of Sussex, Brighton BN1 9QH, U.K. (e-mail: o.al-kadi@sussex.ac.uk).

D. Watson is with the Department of Informatics, University of Sussex, Brighton BN1 9QH, U.K. (e-mail: desw@sussex.ac.uk).

Color versions of one or more of the figures in this paper are available online at http://ieeexplore.ieee.org.

Digital Object Identifier 10.1109/TBME.2008.919735

TABLE I
SOME STUDIES THAT USED FD FOR TEXTURE ANALYSIS AND CLASSIFICATION

Examined organ	Researchers	Modality	Method used
Lung	Kido et al & [5]	CT	Fractal feature extraction based on DBC
	Uppaluri et al [23]	CT	Using multiple statistics with FD
Liver	Wu et al [25]	US	Extracting multi-threshold FD vector
	Lee et al [22]	US	Fractal feature vector based on M-Band wavelet transform
Breast lesions	Chen et al [26]	US	Fractal feature extraction based on fBm
	Penn et al [27]	MR	Fractal-Interpolation Function (FIF)
	Mavroforakis et al [28]	X-ray	Quantitative approach based on advanced classifier architectures supported by fractal analysis
Blood perfusion in tumor tissue of canine subject	Craciunescu et al [29]	MR	FIF for 3-D tumor perfusion reconstruction

tumors. Therefore, it would be very promising if tumor aggression could be determined with good accuracy through examining its texture from contrast-enhanced (CE) CT images only.

The FD of a structure provides a measure of its texture complexity. For example, if the pixel intensities in a CT image are regarded as the height above a plane, then the intensity surface can be perceived as a rugged surface. Fractals deal with structures that are not exactly Euclidean (i.e., "in-between dimensions") giving the potential for a richer description of the examined surface, resembling in analogy the relation of fuzzy logic to digital logic. Although the FD alone cannot provide sufficient information to indicate the aggression of the tumors, this paper extracts vector basis of FDs for tumor ROIs and correlates them with other clinical factors, investigating whether the texture complexity could be linked to other factors that have already been shown to be capable of predicting the aggression of the examined tumor in its early stages.

This paper describes the research as follows. Section II provides an overview of the notion of fractal dimension. Section III describes the procedures and methodology, followed by experimental results and a discussion in Sections IV and V, respectively. The paper ends in Section VI with a conclusion.

II. THEORETICAL CONCEPTS OF FRACTAL DIMENSION

Mathematically, fractals can be defined as a geometrical set whose Hausdorff–Besicovitch dimension strictly exceeds the topological dimension [13]. The term fractal was first introduced by Benoit Mandelbrot to describe non-Euclidean structures that show self-similarity at different scales. Given that most biological and natural features show discontinuities and fragmentation, they tend to have an FD. Also most of these natural structures are complex and rarely have an exact Euclidean (smooth) shape so that they can be precisely measured.

In Euclidean n-space, a bounded set $\boldsymbol{S}$ can be considered statistically self-similar if $\boldsymbol{S}$ is the union of N_r nonoverlapping subsets with respect to a scaling factor r, each of which is of the form $r(\boldsymbol{S}_n)$ where the N_r and $\boldsymbol{S}_n$ sets are congruent in distribution to $\boldsymbol{S}$. Thus, the Hausdorff–Besicovitch-which is the fractal dimension—of a bounded set $\boldsymbol{S}$ in $\Re^n$ is a real number used to characterize the geometric complexity of $\boldsymbol{S}$ in the same way as length is used as a measurement tool in the Euclidean (discrete) space. Hence, the FD can be computed as follows [13]:

$$\mathrm{FD} = \frac{\log(N_r)}{\log(1/r)} \tag{1}$$

where N_r is the number of self-similar (invariant) shapes and r is the corresponding scaling factor.

Actually, most natural and some mathematical self-similar fractals are random, meaning that they scale in a statistical fashion. The resemblance between shapes seen at different scales in natural fractals—and blood vessels branching in lungs are an example—is usually approximate and are considered to be random rather than self-similar. In theory, the FD of a structure examined should have invariant self-similar fragmented and irregular shapes at all scales of measurement reaching to infinity. Yet, in biological structures, this could only be true for a finite number of scales, depending on the resolution and depth of the acquired image. Therefore, for each examined natural fractal, there is a finite scaling range, such that below and above it, the structure becomes smooth (i.e., Euclidean) or completely rough and non-self-similar (i.e., random).

In order to differentiate between two textures if their FD value was to be identical even though the two textures might not be similar, we need to compute the lacunarity of the FD texture. Lacunarity measures the "lumpiness" of the fractal data, providing metainformation about the computed FD values in the image. The higher the lacunarity, the more inhomogeneous the examined fractal area and vice versa. It is defined in terms of the ratio of the variance over the mean value of the function as in (2), where M and N are the sizes of the FD processed image I [11]

$$L = \frac{1/MN \sum_{m=0}^{M-1} \sum_{n=0}^{N-1} I(m,n)^2}{\left(1/MN \sum_{k=0}^{M-1} \sum_{l=0}^{N-1} I(k,l)\right)^2} - 1. \tag{2}$$

III. METHODOLOGY

The research described in this section is divided into the following phases. The first is the processing phase where all sets of sequences of CE CT images—in digital imaging and communication in medicine (DICOM) format—are acquired for each case and then transformed to FD values for each pixel. The FD transformation resulted in images that were considerably enhanced compared to the original images, making it easier to extract the tumor ROIs. The edges separating different tissue structures and the branching structures of the large blood vessels become more distinguishable. Then comes the fractal analysis phase where the maximum FD average ($\mathrm{FD}_{\mathrm{avg}}$) is computed—an average FD value for the tumor area is calculated for each image

in the time series and the maximum was selected—with its corresponding lacunarity (i.e., the degree of nonhomogeneity). The baseline FD_{avg} is also calculated as the FD of the tumor in the first image in the sequence of DICOM images once the contrast agent starts to diffuse, directly after injection. These values are then correlated with two markers of survival: tumor stage and standardized tumor uptake value of FDG as determined by PET. Finally, the impact of CT acquisition parameters on FD_{avg} and lacunarity is investigated using a phantom structure.

A. Image Acquisition

In the first part, quantitative CE CT was incorporated into 15 patients' (ten males and five females with age 63 $\pm$ 8 years, and having lung cancers greater than 10 mm^2) conventional CT examination performed for clinical tumor-staging. A dynamic sequence of 12 bits per pixel DICOM images of the thorax was acquired at the anatomical level containing the largest transverse dimension of the lung tumor. Fifty milliliters of conventional contrast material (Iopamidol, Bracco, Milan) with an iodine concentration of 370 mg/mL were administered intravenously at 7 mL/s. Patients were instructed to hold their breath during the examination period. Data acquisition started at the time of contrast material injection, and from 1 to 14 one-second images with a slice thickness of 10 mm (120 kV, 300 mAs) were obtained using a cycle time of 3 s.

The second part of the acquisition process required that all patients undergo a PET-FDG scan for acquiring two markers of survival—tumor stage and standardized tumor uptake value of FDG—that gives a better prediction of the tumor state.

Using this approach, we managed to record the change in intensity that the contrast agent contributes as it diffuses in the blood vessels, reaching its peak and eventually when it starts to diffuse away. As the blood vessels become more apparent, the chaotic nature of the blood vessels in the lungs can be examined more easily. Hence, the FD, as it changes during the time when the contrast agent concentration is rising and then falling in the tumor, can be compared with different tumor stages. Moreover, the PET-FDG markers of survival would justify the accuracy of the used texture analysis method.

B. FD Transformation

The acquired CE CT images are transformed to FD images using the differential box-counting (DBC) algorithm [14]–[18] at various different scales then displayed for tumor ROI identification, followed by texture analysis. The DBC approach is commonly used when dealing with thousands of data values per sample (the images here are all 512 $\times$ 512 pixels in size) [19]. In this study, both the DBC and fractional Brownian motion (fBm) algorithms were in fact initially applied to the images, the DBC algorithm was adopted for subsequent analysis as it performed faster in the FD calculations of the 512 $\times$ 512 CE CT images.

The original DICOM image $I(x, y)$ of size $M \times N$ is transformed to an FD image by applying a varying size nonlinear kernel $w(s, t)$ of size $m \times n$ as in (3) that operates by block processing on the neighboring pixels and finds the difference between the highest $(p_{\max})$ and lowest $(p_{\min})$ intensity pixels

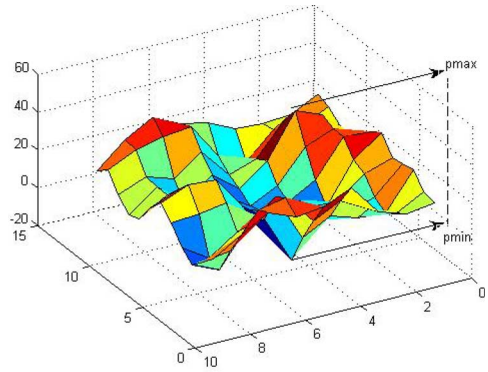

Fig. 1. Surface of the selected ROI shown in Fig. 4 displaying the maximum and minimum peaks.

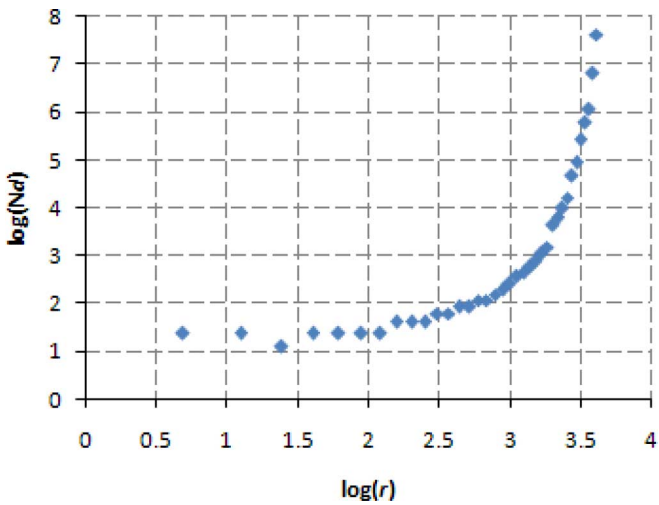

Fig. 2. Scaling factor (r) versus required number of boxes to overlain each image pixel (N_d) in log–log scale.

(see Fig. 1). The two variables a and b are nonnegative integers that are computed in order to center the kernel $w(s, t)$ on pixel p_{xy} in the original image. The kernel is calculated as in (3) and applied as in (4)

$$w(s,t) = \sum_{s=-a}^{a} \sum_{t=-b}^{b} \text{floor}\left[\frac{p_{\max} - p_{\min}}{r}\right] + 1 \qquad (3)$$

where $r = 2, 3, 4, \ldots, j$

$$a = \text{ceil}\left(\frac{m-1}{2}\right), \qquad b = \text{ceil}\left(\frac{n-1}{2}\right)$$

and

$$N_d(x,y,d) = \sum_{s=-a}^{a} \sum_{t=-b}^{b} w(s,t) I(x+s, y+t) \left(\frac{j}{r}\right)^2 \qquad (4)$$

where $d = 1, 2, 3, \ldots, j$–1 is the dimension of matrix $N_d(x, y, d)$ that represents the necessary number of boxes necessary to overlay the image. Empirically, the scaling factor r was chosen to be in the range between 2 and 9. Theoretically, r should represent how much a specific structure of pixels are self-similar to its surrounding. For the 512 mm $\times$ 512 mm CE CT images having a resolution of 12 bits per pixel, Fig. 2

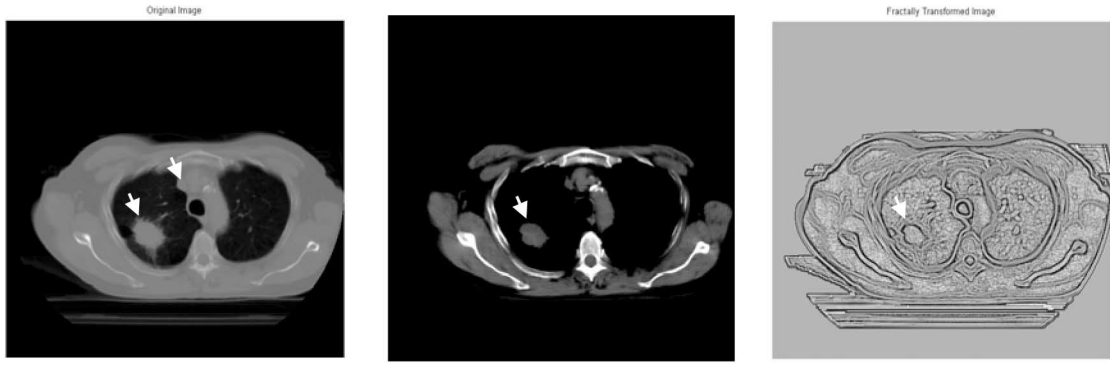

Fig. 3. (a) Original baseline image (slice 1) lower and upper arrows indicating tumor and blood vessel location, respectively. (b) Windowed DICOM image (slice 1). (c) Fractally transformed baseline with image (slice 1).

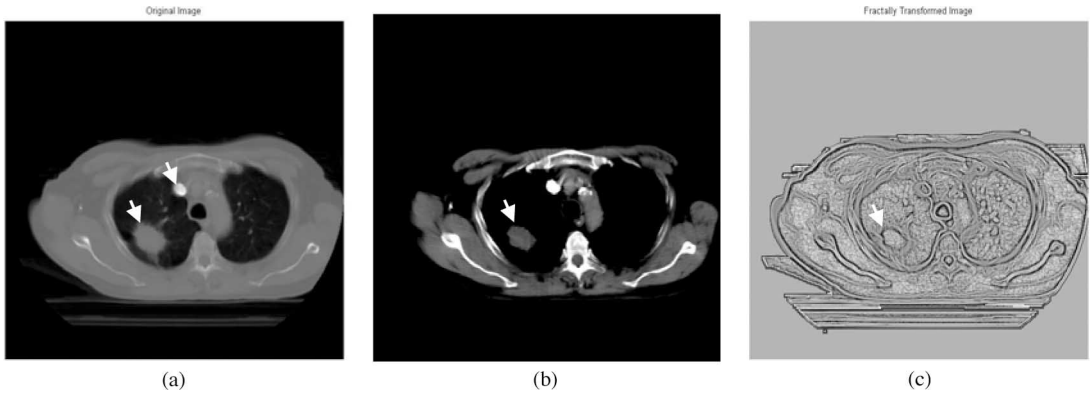

Fig. 4 (a) Original maximum contrast image (slice 5). (b) Windowed DICOM image (slice 5). (c) Fractally transformed maximum contrast image (slice 5).

shows that the best scaling is achieved in this range (i.e., correlation between N_d and r is greater than 0.94) as the FD image starts to become blurry—due to nonlinearity and resolution constraints—if we tend to extend the range much more further that would certainly change the accuracy of the calculated FD value. Similarly choosing a smaller range would result in insufficient surrounding pixels to correctly estimate the FD value. Finally, the slope of the linear regression line of $N_d(x, y, d)$ and r would represent the FD of that pixel. The Appendix describes how the fractal slope was generated.

To further investigate the fractal homogeneity of the lung tumor texture, FD lacunarity was also computed.

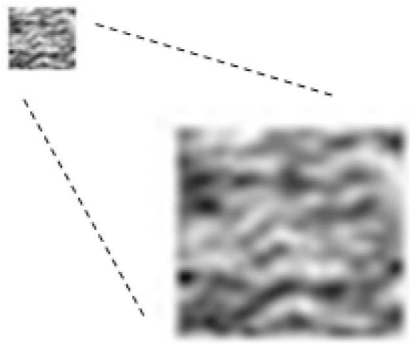

Fig. 5. Selected FD tumor ROI enlarged to show texture.

C. Region of Interest and Feature Extraction

Having the FD-transformed images and under the supervision of a clinical expert, it became comparatively easy to select an ROI that lies within the tumor area for all images in the sequence for each patient. The ROIs were selected manually as using an automated segmentation procedure could not guarantee the texture of the tumor area not to include accidently some surrounding tissue. Fig. 3(a)–(c) shows the baseline CT image (slice 1) once the contrast agent starts to diffuse, before and after FD transformation. In the upper right side of the left lung in Fig. 4(a), it can be seen that the blood vessel became very bright as compared to Fig. 3(a). This corresponds to the point at which the effect of the contrast agent appears to be at its maximum, which varies from one case to another. In this case, it reached its maximum in the fifth slice. The vascularization of the tumor—indicated by the lower white arrow—can be easily distinguished from the surrounding structure, as shown in Fig. 4(c). Figs. 3(b) and 4(b) are the windowed versions of the original DICOM images with the window width (WW) and window gray level (WL) set in Hounsfield units for tumors, which are 300 and 20 HU, respectively. Then the ROIs are extracted for each set (see Fig. 5) by first displaying the first image in the set of images and bounding the examined area by a polygon. We have to ensure that no surrounding tissue is included in

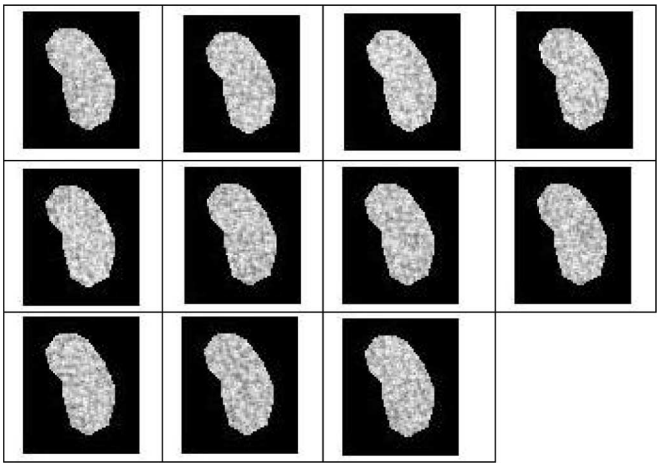

Fig. 6. From left to right—11 ROIs extracted from 11 successive CT images with slice 3 giving the highest FD_{avg}.

TABLE II
SLICES FOR PHANTOM GROUP 3 SHOWING CORRESPONDING CT ACQUISITION PARAMETERS [X-RAY TUBE VOLTAGE (V) AND CURRENT (C)] FOR FRACTAL FEATURES (FD_{AVG} AND LACUNARITY)

Phantom set 3				
Slice	**FD_{avg}**	**Lacunarity**	**V** (kV)	**C** (mAs)
1	2.1898	0.0214	80	100
2	2.1947	0.0199	80	150
3	2.209	0.0178	80	200
4	2.2052	0.0176	80	250
5	2.2183	0.0161	100	150
6	2.2182	0.0161	120	100
7	2.2209	0.0139	120	150
8	2.2026	0.0134	120	200
9	2.1883	0.013	120	250
10	2.2032	0.0135	140	150

this polygon in any of the sequence of images, since respiratory motion may affect the image registration. Subsequently, identical ROIs are extracted from all successive slices. Again all ROIs are visually checked for no inclusion of nearby boundaries due to patient's possible respiratory motion (see Fig. 6). Finally, the average FD is computed for each ROI for each time sequence image for a specific patient and then selecting the maximum FD_{avg} that will be correlated with the already-known tumor stage and FDG value. It should be noted that all procedures in this study have received ethical approval.

D. Impact of CT Tube Voltage and Current on FD_{avg} and Lacunarity

To further investigate what impact the X-ray voltage and tube current parameter might have on the calculated FD texture measures from CE CT images, using a phantom structure, four different data sets with ten slices in each and having a fixed 5-mm thickness was acquired by varying the voltage and tube current for each slice. All 40 slices were processed to get the FD_{avg} and lacunarity features, as shown in Table II for one of the sets. Then, each corresponding slice from each set is placed in a separate group, each group represents a specific

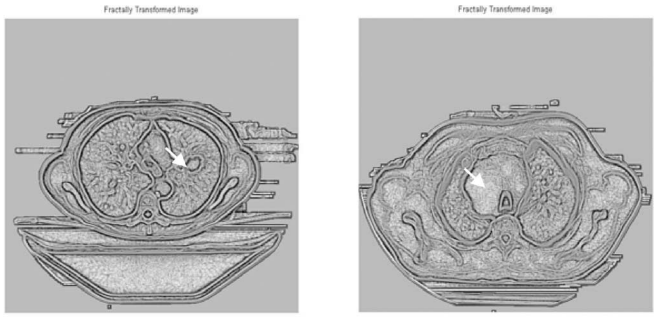

(a) (b)

Fig. 7. Fractally transformed images. (a) Early-stage nonaggressive lung tumor. (b) Advanced stage aggressive lung tumor.

TABLE III
NUMBER OF CASES GREATER THAN THRESHOLD 1.913

Tumor stage	**FD_{avg} >1.913**
1	0%
2	25%
3	66.67%
4	83.3%

slice number giving us a total of ten groups with four slices in each. The standard deviation for each group was computed to see which group (i.e., slice number acquired according to a specific voltage and current value) would represent the least error in the calculation of FD texture measures.

IV. EXPERIMENTAL RESULTS AND EVALUATION

A. Fractal Analysis

Most cases that were diagnosed as aggressive tumors (stages 3 and 4) gave a higher FD_{avg} value as compared to the nonaggressive cases (stage 1). For example, results gave an FD_{avg} value of 2.046 for lung tumor ROI classified as aggressive (i.e., high metabolic) in Fig. 7(a), while Fig. 7(b), classified as nonaggressive (i.e., low metabolic), gave a much lower FD_{avg} value of 1.534.

Choosing the value of 1.913 that is the median of all maximum FD_{avg} values referring to all 15 cases we analyzed to act as a threshold differentiating between aggressive and nonaggressive tumors, Table III shows the most aggressive tumors (stages 3 and 4) that are all highly metabolic lie above this threshold, with 83.3% of stage four cases above the threshold. This threshold could be used in CT scan software systems that would assist the physician in distinguishing between aggressive and nonaggressive cases.

Also, as shown in Table IV for every tumor stage, the higher the FD, the lower the corresponding lacunarity value, and also shows greater homogeneity. This gives some indication that aggressive tumors tend to be more homogeneous. Moreover, the average lacunarity over the whole set of image sequence referring to each case correlates strongly with FDG ($\rho = -0.6273$ and $p = 0.0123$).

TABLE IV
FD TEXTURE ANALYSIS DATA FOR ALL 15 CASES

Patient	Tumor stage	No. of slices	Area (cm^2)	FDG	maxFD_{avg}	Lacunarity	Baseline FD_{avg}	ΔFD
Case 1	2^	11	1.439	4.78	1.7997 (5)*	0.0457	1.4937	0.306
Case 2	4	11	1.072	5.54	1.9214 (1)	0.0275	1.9214	-0.367
Case 3	4	12	7.533	7.86	1.8330 (1)	0.0450	1.8330	-0.162
Case 4	3	13	32.982	9.12	2.0341 (1)	0.0201	2.0341	-0.069
Case 5	4	11	42.123	6.41	2.0061 (2)	0.0268	1.9649	-0.055
Case 6	1	14	3.555	3.58	1.5344 (6)	0.1333	1.5223	0.012
Case 7	2	11	11.850	6.33	1.9131 (2)	0.0430	1.9106	-0.181
Case 8	4	11	19.298	10.36	1.9992 (1)	0.0235	1.9992	-0.216
Case 9	1	11	3.300	2.8	1.7890 (1)	0.0415	1.7890	-0.254
Case 10	3	13	12.160	6.44	1.9687 (1)	0.0348	1.9687	-0.178
Case 11	4	11	28.044	9.75	2.0461 (1)	0.0171	2.0461	-0.152
Case 12	4	13	5.050	5.82	1.9114 (3)	0.0553	1.8708	-0.311
Case 13	3	11	3.611	6.26	1.6374 (2)	0.1411	1.5630	-0.122
Case 14	2	13	26.154	6.35	2.0034 (2)	0.0256	1.9550	-0.087
Case 15	2	11	6.546	7.83	1.8575 (2)	0.0273	1.8444	-0.222

^ 1 for early stage while 4 for advanced stage
* indicates the occurrence in slice number (n)

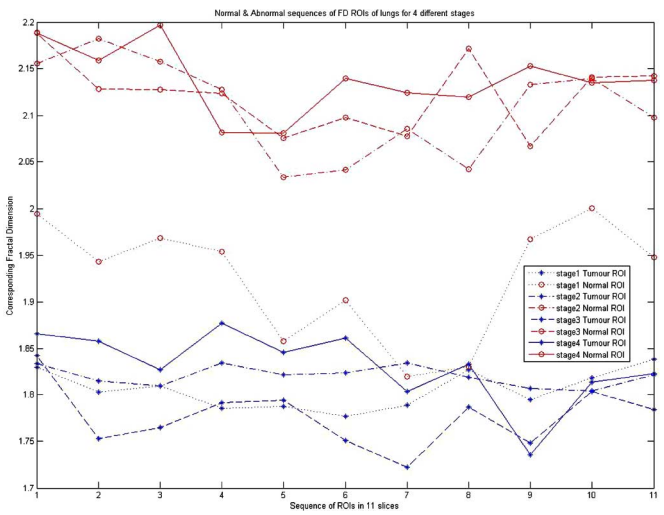

Fig. 8. Different sequence of FD ROIs, representing four different stage tumors and four normal, upper four sequences are the lung tumor FD ROIs that represent four different stages while the lower four sequences are corresponding normal FD ROIs.

Moreover, Fig. 8 shows an 11-sequence of eight different FD ROIs with the starting slice 1 acting as the baseline image and slice 11 is when the contrast agent has completely diffused. These FD ROIs are classified as four normal and four vascularized (i.e., tumor) that refer to the four different stages of lung tumors. For each tumor FD ROI, a corresponding normal region is selected from the normal part of the lung; by this, we have two ROIs from each case.

It can be seen that nonaggressive tumors (e.g., stage 1) such as the fifth dotted line from down in Fig. 8 tend to have a different range than other tumors—upper three lines in Fig. 8—where their FD_{avg} values are all above 2, with stage 4—first solid line from up—achieving the highest FD value. Also, normal ROIs

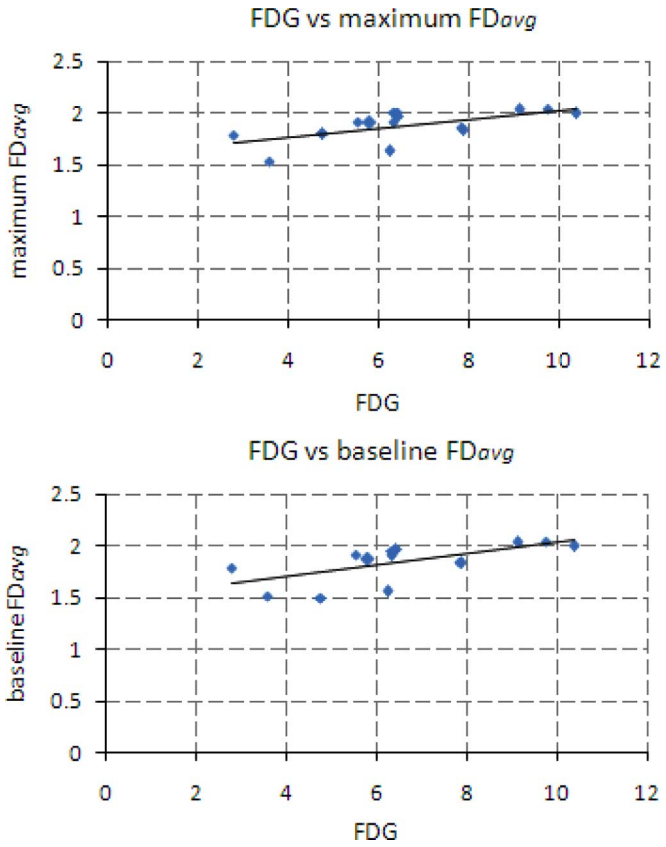

Fig. 9. Significant correlation between standard tumor uptake of FDG with maximum and baseline FD_{avg}.

were included in the graph for clarification purposes to make sure that their FD_{avg} ranges values are completely different to those of the tumor, especially if the baseline or maximum FD_{avg} was used for classification.

B. Statistical Tests

Using the Spearman rank-order correlation test, the tumor baseline FD_{avg} and the maximum FD_{avg} were correlated with the corresponding lung tumor stages, giving a correlation coefficient of 0.537 and 0.52 with a significance level of 0.0387 and 0.0468 for two-tailed p-value, respectively.

Also, using linear regression, the tumor maximum FD_{avg} and baseline FD_{avg} correlated with tumor uptake of FDG as determined by PET, giving $\rho = 0.63, p = 0.012$, and $\rho = 0.634, p = 0.011$, respectively (see Fig. 9).

A summary of the complete results for all sets of sequences of images corresponding to 15 patients is given in Table IV. The table shows for each patient the number of slices acquired, tumor stage, area of tumor, computed FDG value, the maximum FD_{avg}, and its corresponding lacunarity, as well as the baseline FD_{avg}, and the behavioral direction ΔFD. ΔFD simply represents the difference between the minimum and the maximum FD_{avg} rate of change with respect to time. It shows that only two cases from all 15 had a positive trend and these cases were classified as stage 1 (i.e., early stage). This needs to be further investigated through applying this procedure to more cases to see whether

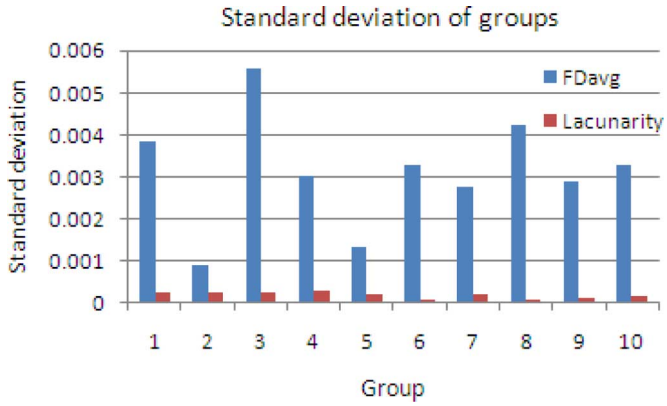

Fig. 10. Standard deviation of fractal features for groups of similar phantom slices acquired under specific voltage (in kilovolts) and tube current (in milliamperes) CT parameters.

ΔFD for early-stage tumors in time series CE CT images tend to change in a different way.

C. Phantom Tests

Group 2 for FD_{avg} and group 6 for lacunarity gave the least error, as shown in Fig. 10. From Table II, the corresponding voltage and current parameters for FD_{avg} and lacunarity are 80 kV and 150 mAs, and 120 kV and 100 mAs, respectively.

V. Discussion

This study aims to specify a lung tumor aggression index to assist in better classifying and staging lung tumors from CT images without the need of a PET scan. Results show that selecting tumor ROIs from slices that have the maximum and baseline FD_{avg} can improve stage prediction.

The presumed reason behind the observation that nonaggressive cancers have a lower maximum FD_{avg} value as compared to the aggressive cancers is that given which blood vessels in the lungs appear as fractals, the action of administering a contrast agent will enhance the intensity of the blood vessels in the image, as we are viewing the image from an FD perspective. We would expect that the FD_{avg} would increase with time reaching a maximum at some point near the middle image of the sequence, after the tumor has been infused by the contrast agent and before it has started diffusing away. Although this is true for ROIs from nonaggressive cancers, as the blood vessels in that region still maintain some of its fractal characteristics, in the aggressive tumors, the general shape of the blood vessels has been altered and deformed in such a way, becoming very rough, resulting in some increase in the original blood vessels' fractal characteristics. This increase in roughness contributed to the observed maximum FD_{avg} value in these cases as compared to the nonaggressive cases.

Regarding the selection of the DBC algorithm, Penn and Loew [20] studied the effectiveness of the DBC algorithm and the power spectrum that is based on an fBm algorithm, in performing texture analysis to separate classes of blood cell images. They suggest that these approaches may be inaccurate if applied to data-limited, low-resolution images. We overcame this problem by using high-resolution CE CT scans for image acquisition. The images that we applied the DBC algorithm to had a resolution of 12 bits per pixel with no obvious distorting noise, thus ruling out any possibility of miscalculations in the FD computations due to poor resolution.

The DBC algorithm transformed the image to the FD approximately 2.5 times faster than the fBm approach; therefore, it was adopted for subsequent analysis. In order to reduce processing time still further, we could have transformed just the ROIs to the FD values, and perform the subsequent fractal analysis on these data. However, as the FD transformation is a very effective edge enhancer technique [21], we decided to enhance the acquired image first in order to help identify the tumor region precisely, ruling out any possible inclusion of any adjacent tissue boundaries into the FD tumor calculations. This is especially important as we are working with multiple CE CT images acquired over time where the tumor area can change in size and position due to the patient's respiratory movements. Hence, we needed to balance the tradeoff between choosing the smallest possible area size for the whole sequence of CE CT images not including any nearby normal tissue, and making sure that the ROI is sufficiently large to obtain an accurate FD estimate of the examined tumor region.

Additionally, Lee *et al.* [22] used a kernel that calculates the standard deviation multiplied by two inside the operating box instead of the difference between the maximum and minimum intensities divided by the scaling factor in order to reduce the effect of noise in the acquired images. Although the FD tends to not enhance noise since it is a roughness representation of the surface [21], the CE CT images that we processed had a high spatial resolution, comparatively free from visible noise. So using the standard deviation method on high-quality images could result in loss of some relevant information from the processed image; it was therefore more appropriate to use the differential method for our case.

Others used the same modality for texture analysis. Kido *et al.* [5], [6] and Uppaluri *et al.* [23] showed that FD for lung CT images could be useful in differentiating between normal and abnormal lung tissues for nontumor cases. In contrast, our focus was specific to only abnormality trying to differentiate between lung tumors upon their aggression. Also, we used time sequence CE CT images to more reliably estimate the FD while the previously mentioned two studies operated on ordinary CT images. This assisted us in identifying to what extent we can extend the range of the scaling factor confidently in the DBC algorithm so that the computed FD for each pixel would have more fidelity. Furthermore, to assess the accuracy of the computed texture measures, we correlated the FD_{avg} values for ROIs with the medical key factors, FDG and staging, that were measured using PET. Hence, we can better estimate the stage and aggression state of the examined tumor from CT images.

Lacunarity of the FD-transformed ROI was measured to further differentiate between ROIs that showed similar FD values. Moreover, it was shown that calibrating the CT voltage and tube current parameters with the values presented in the experimental results section would assist in calculating the FD

texture measure more accurately, yet it needs to be verified on real CE CT lung images to check consistency.

Nevertheless, the analysis of tumors less than 10 mm^2 in size in this study would have been possible, but the inherent noise resolution of CT would make such analysis unreliable. The results would have been better improved if CT slice thickness was thinner and the data acquired with a higher resolution (e.g., 16 bits per pixel). This could have made possible the investigation of tumors having a size smaller than 10 mm^2. However, the likelihood of increased noise when acquired images are of higher resolution reduces the accuracy of the texture estimates.

VI. Conclusion

A fractal analysis of aggressive and nonaggressive lung tumors based on correlation with other related key medical factors was proposed in this study. Previous work done was mainly concerned with distinguishing normal and abnormal tissue, while this technique assesses the potential for tumor FD measurements through CE CT images to provide an indication of tumor aggression. After specifying a threshold, most late-stage cases resulted in a higher $\mathrm{FD}_{\mathrm{avg}}$ as compared to the early cases. Moreover, there was a significant correlation between tumor stage severity and FDG—acquired by PET scan—with the baseline and maximum value of $\mathrm{FD}_{\mathrm{avg}}$ occurring in one of the time sequence CE CT images. This implies that the $\mathrm{FD}_{\mathrm{avg}}$ value computed from the tumor ROI could serve as a prognostic marker assisting in deciding whether the tumor should be further investigated by a PET scan.

Usually aggressive cancers are dealt with by nonsurgical procedures such as chemotherapy, since surgical intervention can provoke the tumor to spread and grow faster. These preliminary results could assist physicians in noninvasively investigating the behavior of the examined lung tumor from time sequence CE CT images with no need of biopsy to be taken. It was also shown that through selecting the appropriate CT-acquisition parameters can play a significant role in improving the computation accuracy of the FD.

Studying the effect of CT image reconstruction algorithms on $\mathrm{FD}_{\mathrm{avg}}$ and the application of this technique to other imaging modalities (MRI and ultrasound) and for brain tumors is being investigated.

Appendix

After computing the multidimensional matrix $N_d(x, y, d)$, where the first dimension d represents the original image after it has been filtered by kernel of scale 2, and the second dimension represents the image filtered by kernel of scale 3, etc., until reaching the highest scale j

$$N_d(x,y,d) = \begin{pmatrix} p_{11d} & p_{12d} & \cdots & \cdots & p_{1Nd} \\ p_{21d} & p_{22d} & \cdots & \cdots & p_{2Nd} \\ \vdots & \vdots & \ddots & & \vdots \\ \vdots & \vdots & & \ddots & \vdots \\ p_{M1d} & p_{M2d} & \cdots & \cdots & p_{MNd} \end{pmatrix} \quad \text{(A1)}$$

where M and N are the sizes of the processed image, and $d = 1, 2, 3, \ldots, j$–1 is the dimension of the matrix $N_d(x, y, d)$.

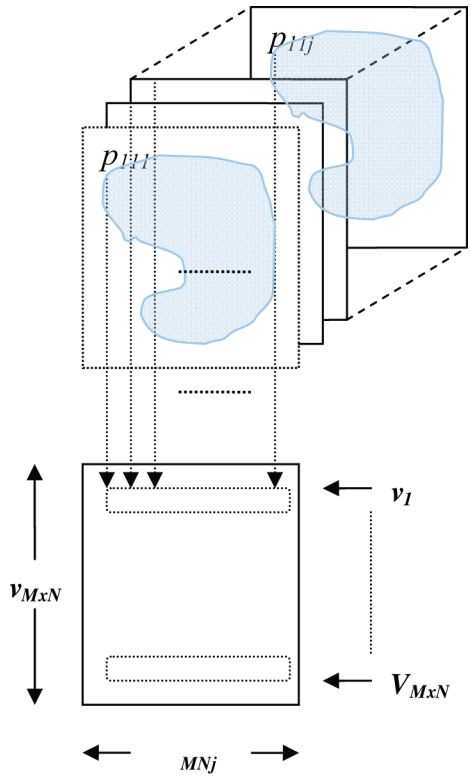

Fig. 11. Obtaining an array of row vectors from a multidimensional array $N_d(x, y, d)$.

Given $N_d(x, y, d)$ that represents the number of boxes necessary to cover the whole image, we perform the log operation on all elements of $N_d(x, y, d)$ and the corresponding scaling factor r. One of the advantages of the logarithm operation is that it expands the values of the dark pixels in the image while compressing the higher brighter level values; also it compresses the dynamic range of images with large variations in pixel values [24].

After applying the logarithmic operations, each element from each array in $N_d(x, y, d)$ will be saved in a new row vector v.

That is, the first element in all arrays of $N_d(x, y, d)$ will compose vector v_1, and all second elements will compose vector v_2, etc., as shown in (A2). This process is depicted in Fig. 11.

$$\begin{pmatrix} v_1 \\ v_2 \\ v_3 \\ \vdots \\ v_{M\times N} \end{pmatrix} = \begin{pmatrix} p_{111} & p_{112} & \cdots & \cdots & p_{11j} \\ p_{121} & p_{122} & \cdots & \cdots & p_{12j} \\ \vdots & \vdots & \ddots & & \vdots \\ \vdots & \vdots & & \ddots & \vdots \\ p_{MN1} & p_{MN2} & \cdots & \cdots & p_{MNj} \end{pmatrix}. \quad \text{(A2)}$$

Finally, by having the number of boxes required to cover the entire image area $N_d(x, y, d)$ with the scaling factor r, we can determine the slope b_{xy} of the least square linear regression line

by computing the sums of squares:

$$S_{kk} = \sum_{l=1}^{j-1} r^2 - \frac{\left(\sum_{l=1}^{j-1} r\right)^2}{j-1} \tag{A3}$$

$$S_{kv} = \sum_{l=1}^{j-1} rv - \frac{\left(\sum_{l=1}^{j-1} r\right)\left(\sum_{l=1}^{j-1} v\right)}{j-1}. \tag{A4}$$

The slope of the linear regression line gives the FD:

$$\mathrm{FD}(x,y) = b_{xy} = \sum_{x=1}^{M}\sum_{y=1}^{N} \frac{S_{kv}}{S_{kk}} = \begin{pmatrix} b_{11} & b_{12} & \cdots & \cdots & b_{1N} \\ b_{21} & b_{22} & \cdots & \cdots & b_{2N} \\ \vdots & \vdots & \ddots & & \vdots \\ \vdots & \vdots & & \ddots & \vdots \\ b_{M1} & b_{M2} & \cdots & \cdots & b_{MN} \end{pmatrix}. \tag{A5}$$

ACKNOWLEDGMENT

The authors would like to thank the Clinical Imaging Science Center, Brighton, Sussex Medical School, and Prof. K. Miles for the provision of medical data, and the anonymous reviewers for their valuable comments.

REFERENCES

[1] G. K. von Schulthess, H. C. Steinert, and T. F. Hany, "Integrated PET/CT-3: Current applications and future directions," *Radiology*, vol. 238, pp. 405–422, 2006.

[2] A. P. Meert, M. Paesmans, B. Martin, P. Delmotte, T. Berghmans, J. M. Verdebout, J. J. Lafitte, C. Mascaux, and J. P. Sculier, "The role of microvessel density on the survival of patients with lung cancer: A systematic review of the literature with meta-analysis," *Br. J. Cancer*, vol. 87, pp. 694–701, 2002.

[3] M. Matsuki, S. Noma, Y. Kuroda, K. Oida, T. Shindo, and Y. Kobashi, "Thin-section CT features of intrapulmonary lymph nodes," *J. Comput. Assist. Tomogr.*, vol. 25, pp. 753–756, 2001.

[4] I. Petkovska, S. K. Shah, M. F. McNitt-Gray, J. G. Goldin, M. S. Brown, H. J. Kim, K. Brown, and D. R. Aberle, "Pulmonary nodule characterization: A comparison of conventional with quantitative and visual semi-quantitative analyses using contrast enhancement maps," *Eur. J. Radiol.*, vol. 59, pp. 244–252, 2006.

[5] S. Kido, K. Kuriyama, M. Higashiyama, T. Kasugai, and C. Kuroda, "Fractal analysis of internal and peripheral textures of small peripheral bronchogenic carcinomas in thin-section computed tomography: Comparison of bronchioloalveolar cell carcinomas with nonbronchioloalveolar cell carcinomas," *J. Comput. Assist. Tomogr.*, vol. 27, pp. 56–61, 2003.

[6] S. Kido, K. Kuriyama, M. Higashiyama, T. Kasugai, and C. Kuroda, "Fractal analysis of small peripheral pulmonary nodules in thin-section CT—Evaluation of the lung–nodule interfaces," *J. Comput. Assist. Tomogr.*, vol. 26, pp. 573–578, 2002.

[7] N. Mihara, K. Kuriyama, S. Kido, C. Kuroda, T. Johkoh, H. Naito, and H. Nakamura, "The usefulness of fractal geometry for the diagnosis of small peripheral lung tumors," *Nippon Acta Radiol.*, vol. 58, pp. 148–151, 1998.

[8] N. F. Vittitoe, J. A. Baker, and C. E. Floyd, "Fractal texture analysis in computer-aided diagnosis of solitary pulmonary nodules," *Acad. Radiol.*, vol. 4, pp. 96–101, 1997.

[9] J. Peiss, M. Verlande, W. Ameling, and R. W. Gunther, "Classification of lung tumors on chest radiographs by fractal texture analysis," *Invest. Radiol.*, vol. 31, pp. 625–629, 1996.

[10] Z. C. Chen, F. Tang, Z. Y. Zhou, D. Z. Jiang, and Y. Jiang, "Texture characteristic of CT image for lung parenchyma based on fractal dimension," in *Proc. 3rd Int. Symp. Instrum. Sci. Technol.*, 2004, vol. 3, pp. 716–720.

[11] M. Petrou and P. G. Sevilla, *Image Processing: Dealing With Texture*. New York: Wiley, 2006.

[12] Y. Nakamoto, T. Higashi, H. Sakahara, N. Tamaki, M. Kogire, M. Imamura, and J. Konishi, "Contribution of PET in the detection of liver metastases from pancreatic tumours," *Clin. Radiol.*, vol. 54, pp. 248–252, 1999.

[13] B. B. Mandelbrot, *Fractal Geometry of Nature*. San Francisco, CA: Freeman, 1982.

[14] N. Sarkar and B. B. Chaudhuri, "An efficient differential box-counting approach to compute fractal dimension of image," *IEEE Trans. Syst., Man, Cybern.*, vol. 24, no. 1, pp. 115–120, Jan. 1994.

[15] S. Buczkowski, S. Kyriacos, F. Nekka, and L. Cartilier, "The modified box-counting method: Analysis of some characteristic parameters," *Pattern Recognit.*, vol. 31, pp. 411–418, 1998.

[16] J. M. Keller, S. Chen, and R. M. Crownover, "Texture description and segmentation through fractal geometry," *Comput. Vis. Graph. Image Process.*, vol. 45, pp. 150–166, 1989.

[17] J. Feng, W.-C. Lin, and C.-T. Chen, "Functional box-counting approach to fractal dimension estimation," in *Proc. 13th Int. Conf. Pattern Recognit. (ICPR 1996)*, pp. 854–858.

[18] S. S. Chen, J. M. Keller, and R. M. Crownover, "On the calculation of fractal features from images," *IEEE Trans. Pattern Anal. Mach. Intell.*, vol. 15, no. 10, pp. 1087–1090, Oct. 1993.

[19] C. J. Traina, A. Traina, L. Wu, and C. Faloutsos, "Fast feature selection using fractal dimension," in *Proc. 15th Braz. Symp. Databases*, Oct. 2000, pp. 158–171.

[20] A. I. Penn and M. H. Loew, "Estimating fractal dimension with fractal interpolation function models," *IEEE Trans. Med. Imag.*, vol. 16, no. 6, pp. 930–937, Dec. 1997.

[21] C. C. Chen, J. S. Daponte, and M. D. Fox, "Fractal feature analysis and classification in medical imaging," *IEEE Trans. Med. Imag.*, vol. 8, no. 2, pp. 133–142, Jun. 1989.

[22] W.-L. Lee, Y. Chen, and K. Hsieh, "Ultrasonic liver tissue classification by fractal feature vector based on M-band wavelet transform," *IEEE Trans. Med. Imag.*, vol. 22, no. 3, pp. 382–392, Mar. 2003.

[23] R. Uppaluri, T. Mitsa, and J. R. Galvin, "Fractal analysis of high-resolution CT images as a tool for quantification of lung diseases," in *Proc. Physiol. Funct. Multidimensional Images—Med. Imag. 1995*, San Diego, CA, vol. 2433. Bellingham, WA: SPIE, pp. 133–142.

[24] R. C. Gonzales and R. E. Woods, *Digital Image Processing*, 2nd ed. Englewood Cliffs, NJ: Prentice-Hall, 2002.

[25] C. M. Wu and Y. C. Chen, "Multithreshold dimension vector for texture analysis and its application to liver-tissue classification," *Pattern Recognit.*, vol. 26, pp. 137–144, 1993.

[26] D. R. Chen, R. F. Chang, C. J. Chen, M. F. Ho, S. J. Kuo, S. T. Chen, S. J. Hung, and W. K. Moon, "Classification of breast ultrasound images using fractal feature," *Clin. Imag.*, vol. 29, pp. 235–245, 2005.

[27] A. I. Penn, L. Bolinger, M. D. Schnall, and M. H. Loew, "Discrimination of MR images of breast masses with fractal-interpolation function models," *Acad. Radiol.*, vol. 6, pp. 156–163, 1999.

[28] M. E. Mavroforakis, H. V. Georgiou, N. Dimitropoulos, D. Cavouras, and S. Theodoridis, "Mammographic masses characterization based on localized texture and dataset fractal analysis using linear, neural and support vector machine classifiers," *Artif. Intell. Med.*, vol. 37, pp. 145–162, 2006.

[29] O. I. Craciunescu, S. K. Das, J. M. Poulson, and T. V. Samulski, "Three-dimensional tumor perfusion reconstruction using fractal interpolation functions," *IEEE Trans. Biomed. Eng.*, vol. 48, no. 4, pp. 462–473, Apr. 2001.

Omar S. Al-Kadi (M'02) received the B.Sc. degree in biomedical engineering from Cairo University, Cairo, Egypt, in 2001, and the M.Sc. degree in information technology from University of Canberra, Canberra, Australia, in 2003. He is currently working toward the Ph.D. degree in engineering at the University of Sussex, Brighton, U.K.

He worked as a lecturer in King Abdullah II School for Information Technology, Amman, Jordan, from 2004 to 2005. His current research interests include image processing (texture analysis, image classification, and image segmentation), computer vision, and pattern recognition.

D. Watson, photograph and biography not available at the time of publication.